

## ARTICLE IN PRESS – J. Appl. Cryst.

JOURNAL OF  
APPLIED  
CRYSTALLOGRAPHY

ISSN 1600-5767

## Tomographic X-ray scattering based on invariant reconstruction – analysis of the 3D nanostructure of bovine bone

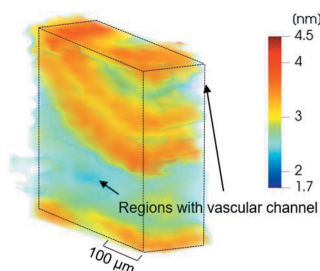
**Proof instructions**

Proof corrections should be returned by **23 February 2021**. After this period, the Editors reserve the right to publish your article with only the Managing Editor's corrections.

Please



- (1) Read these proofs and assess whether any corrections are necessary.
- (2) Check that any technical editing queries highlighted in **bold underlined** text have been answered.
- (3) Send corrections by e-mail to [ls@iucr.org](mailto:ls@iucr.org). Please describe corrections using plain text, where possible, giving the line numbers indicated in the proof. Please do not make corrections to the pdf file electronically and please do not return the pdf file. If no corrections are required please let us know.

Your article appears to qualify for open-access publication at no charge under a transformative deal with your institution. To purchase printed offprints, please complete the attached order form and return it by e-mail.

**Please check the following details for your article**

Thumbnail image for contents page

**Synopsis:** Please provide a synopsis (of not more than two sentences) to appear in the Contents listing of the journal.

**Abbreviated author list:** De Falco, P.; Weinkamer, R.; Wagermaier, W.; Li, C.; Snow, T. ( 0000-0001-7146-6885); Terrill, N.J. ( 0000-0002-8783-1282); Gupta, H.S.; Goyal, P.; Stoll, M.; Benner, P.; Fratzl, P.

**Keywords:** SAXS; tomography; bovine bone; fibrolamellar unit; *T* parameter; small-angle X-ray scattering; scattering tomography; fibrolamellar bone

**Open-access:** Your article appears to qualify for open-access publication at no charge under a transformative deal with your institution.

**How to cite your article in press**

Your article has not yet been assigned page numbers, but may be cited using the doi:

De Falco, P., Weinkamer, R., Wagermaier, W., Li, C., Snow, T., Terrill, N.J., Gupta, H.S., Goyal, P., Stoll, M., Benner, P. et al. (2021). *J. Appl. Cryst.* **54**, <https://doi.org/10.1107/S1600576721000881>.

You will be sent the full citation when your article is published and also given instructions on how to download an electronic reprint of your article.



# Tomographic X-ray scattering based on invariant reconstruction – analysis of the 3D nanostructure of bovine bone

Paolino De Falco,<sup>a</sup> Richard Weinkamer,<sup>a\*</sup> Wolfgang Wagermaier,<sup>a</sup> Chenghao Li,<sup>a</sup> Tim Snow,<sup>b</sup> Nicholas J. Terrill,<sup>b</sup> Himadri S. Gupta,<sup>c</sup> Pawan Goyal,<sup>d</sup> Martin Stoll,<sup>d,e</sup> Peter Benner<sup>d</sup> and Peter Fratzl<sup>a\*</sup>

Received 8 September 2020

Accepted 25 January 2021

Edited by D. I. Svergun, European Molecular Biology Laboratory, Hamburg, Germany

**Keywords:** SAXS; tomography; bovine bone; fibrolamellar unit; *T* parameter; small-angle X-ray scattering; scattering tomography; fibrolamellar bone.

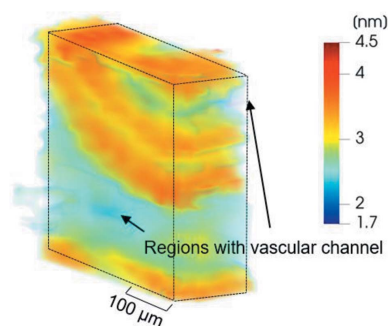
<sup>a</sup>Department of Biomaterials, Max Planck Institute of Colloids and Interfaces, Potsdam 14476, Germany, <sup>b</sup>Diamond Light Source Ltd., Diamond House, Harwell Science and Innovation Campus, Didcot, Oxfordshire OX11 0DE, United Kingdom, <sup>c</sup>School of Engineering and Materials Science, Queen Mary University of London, London E1 4NS, United Kingdom, <sup>d</sup>Max Planck Institute for Dynamics of Complex Technical Systems, Sandtorstrasse 1, Magdeburg 39106, Germany, and <sup>e</sup>Department of Mathematics, TU Chemnitz, Reichenhainer Strasse 41, Chemnitz 09126, Germany. \*Correspondence e-mail: richard.weinkamer@mpikg.mpg.de, fratzl@mpikg.mpg.de

Small-angle X-ray scattering (SAXS) is an effective characterization technique for multi-phase nanocomposites. The structural complexity and heterogeneity of biological materials require the development of new techniques for the 3D characterization of their hierarchical structures. Emerging SAXS tomographic methods allow reconstruction of the 3D scattering pattern in each voxel but are costly in terms of synchrotron measurement time and computer time. To address this problem, an approach has been developed based on the reconstruction of SAXS invariants to allow for fast 3D characterization of nanostructured inhomogeneous materials. SAXS invariants are scalars replacing the 3D scattering patterns in each voxel, thus simplifying the 6D reconstruction problem to several 3D ones. Standard procedures for tomographic reconstruction can be directly adapted for this problem. The procedure is demonstrated by determining the distribution of the nanometric bone mineral particle thickness (*T* parameter) throughout a macroscopic 3D volume of bovine cortical bone. The *T* parameter maps display spatial patterns of particle thickness in fibrolamellar bone units. Spatial correlation between the mineral nanostructure and microscopic features reveals that the mineral particles are particularly thin in the vicinity of vascular channels.

## 1. Introduction

Many biological materials incorporate nanoscopic mineral particles into an organic matrix, thereby reconciling conflicting material properties like strength and toughness (Weinkamer & Fratzl, 2016; Ritchie, 2011; Meyers *et al.*, 2008). From both a biomedical (Xi *et al.*, 2018; Milovanovic *et al.*, 2015) and bio-inspired materials (Bouville *et al.*, 2014; Studart, 2013) perspective, an important example is bone, which is a nanocomposite of stiff inorganic apatite particles embedded in a softer collagenous matrix (Weiner & Wagner, 1998; Fratzl & Weinkamer, 2007). The mineral particles in bone have roughly the shape of thin and elongated platelets with a thickness of 2–5 nm.

The characteristics of the mineral particles not only influence the mechanical performance but also provide hints about changes in bone physiology (Pathi *et al.*, 2011). Previous work showed that the aspect ratio and staggered arrangement of the mineral particles affect the mechanical properties of bone (Jäger & Fratzl, 2000; Xi *et al.*, 2018; Bar-On & Wagner, 2013). In general, the thickness of the mineral particles can be viewed



as an indication of tissue age and normally correlates with the degree of mineralization (Zizak *et al.*, 2003; Roschger *et al.*, 2001; Fratzl *et al.*, 1991), except in the case of *osteogenesis imperfecta*, the brittle bone disease (Fratzl-Zelman *et al.*, 2014). He *et al.* (2017) found that regions affected by cancer metastasis in mouse models contain thinner and less oriented mineral particles compared with healthy bone.

The high contrast in electron density between the inorganic and organic components in bone makes scattering techniques an attractive approach to characterize the mineral particles (Rinnerthaler *et al.*, 1999; Pabisch *et al.*, 2013). A particularly powerful approach is 2D scanning small-angle X-ray scattering (SAXS), where an X-ray beam is used to scan the sample and provides maps of the local mineral nanostructure with a spatial resolution of several micrometres or even less (Pabisch *et al.*, 2013; Paris *et al.*, 2000). The data obtained in this way are 4D, with two real-space dimensions corresponding to the mapping by scanning of the X-ray beam, and another two from the 2D SAXS patterns that correspond to planar sections through reciprocal space.

For a number of research questions a higher-dimensional mapping of mineral characteristics would be desirable. A way of increasing the dimensionality of the information is to collect 3D scattering patterns using a thin sample, but measuring the scattering signal under different angles by rotating the sample. Here the data are quasi-2D in real space but with three dimensions in reciprocal space. Combined SAXS and wide-angle X-ray scattering (WAXS) were used to investigate the crystalline and morphological texture of mineral particles in human vertebrae, showing a close relationship between the *c*-axis orientation and the orientation distribution of the mineral platelets, the plate normal being perpendicular to the *c* axis (Jaschouz *et al.*, 2003). In that study, it was shown that the mineral platelets are aligned with the collagen fibers along the trabecula axis. In synchrotron scanning SAXS/WAXS with a beam size of 1  $\mu\text{m}$ , it was demonstrated that mineral platelets in human osteonal bone change their orientation over a length scale of approximately the thickness of a lamella of  $\sim 5\text{--}10\ \mu\text{m}$  (Seidel *et al.*, 2012; Wagermaier *et al.*, 2006), in agreement with the previously proposed rotated twisted plywood structure (Weiner *et al.*, 1999). This technique can be combined with serial sectioning and scanning the slices under various angles. The result of such an experiment was a full 6D data set with a 3D map of 3D SAXS patterns for a human trabecula (Georgiadis *et al.*, 2016), where results about ultrastructural 3D orientation were confirmed using polarized light microscopy (Georgiadis *et al.*, 2015).

An alternative approach to serial sectioning is SAXS tomography. Instead of reconstructing the attenuation coefficients as in standard microcomputed tomography, the aim here is to measure a bulk sample under different directions of the beam and to reconstruct 3D SAXS patterns in a 3D volume. Under the assumption of structural isotropy, reconstructions of the 1D SAXS pattern were performed for samples like injected polymers (Schroer *et al.*, 2006), nanoporous glass (Feldkamp *et al.*, 2009) and rat brains (Jensen *et al.*, 2011). Only recently was the full reconstruction of the

spatially heterogeneous anisotropic ultrastructure in bone (Liebi *et al.*, 2015) and tooth (Schaff *et al.*, 2015) achieved.

In SAXS measurements the sample is rotated around many different rotational axes. The reconstruction of the obtained 6D data set is computationally intensive and becomes tractable by assuming certain symmetries in the data (tensor tomography) and by fitting the 3D pattern by spherical harmonics (Liebi *et al.*, 2015). Another approach also preserves oriented scattering information by the introduction of virtual scattering axes (Schaff *et al.*, 2015). The application of regularization strategies during reconstruction can save experimental data acquisition time (Liebi *et al.*, 2018) and stronger assumptions on the symmetry of the SAXS pattern can substantially reduce the time needed for reconstruction (Gao *et al.*, 2019).

However, in many instances the full oriented 3D SAXS pattern is not required in every voxel of the reconstructed volume. Instead, information derived from the SAXS patterns such as a Porod-like or Guinier-like analysis (Jensen *et al.*, 2011) is sufficient. Here we develop an approach to reconstruct directly the spatial variation of the particle thickness parameter instead of the spatial variation of full 3D-SAXS patterns. While the original data to be reconstructed consist of a 3D reciprocal-space picture in each real-space voxel, using invariants of the small-angle scattering replaces the 3D-SAXS data by scalars. This effectively reduces the problem to the reconstruction of a 3D matrix of scalars as in conventional X-ray absorption tomography and allows the use of efficient algorithms that have previously been developed for micro-computed tomography.

To test our approach, we chose bovine fibrolamellar bone as our model system, mainly for structural reasons: (i) the cortex

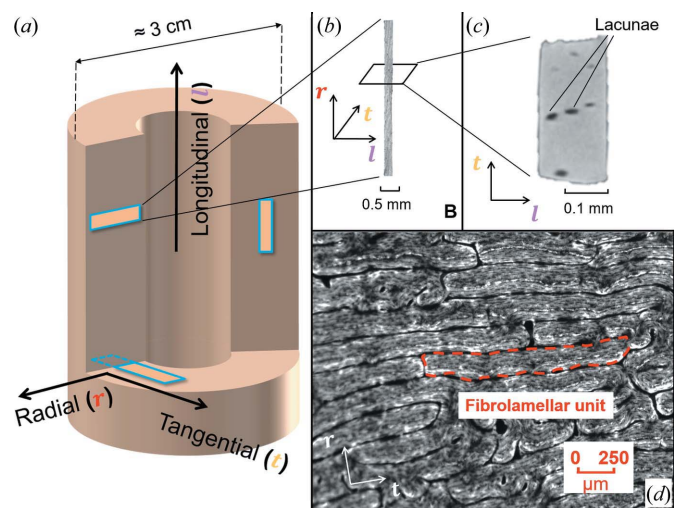


**Figure 1** Macro- and microstructure of femoral bovine bone. (a) A representation of femoral bovine bone at the macroscale, showing the directions of the long axes (radial, tangential and longitudinal) of the measured samples. (b) A  $\mu\text{CT}$  reconstruction of a sample with the long axis aligned to the radial direction of the femur, with an enlargement of a section shown in (c). (d) A light microscopy image showing the arrangement of fibrolamellar units at the microscale. **The red dashed line outlines one such unit.**

of a long bone is structurally anisotropic with a preferred direction along the long axis of the femur, (ii) the bone consists of microscopic fibrolamellar units and these units are arranged in a regular brick-like fashion, with the shortest dimension oriented towards the bone center with a thickness of approximately 200  $\mu\text{m}$  (Fig. 1), and (iii) within the fibrolamellar unit structural features (different layers like the parallel-fibered layer and hypercalciated layer, or vascular channels) are present and large enough to be resolved with our beam size of 10  $\mu\text{m}$ . The structural anisotropy of the fibrolamellar bone is reflected in extremely anisotropic mechanical properties, with the elastic modulus being 20 times higher along the fiber direction than perpendicular to it (Seto *et al.*, 2008). In the transition zone to the neighboring fibrolamellar unit, lamellar bone is found, which again has a preferred fiber orientation along the bone long axis and contains blood vessels. Within both fibrolamellar and lamellar bone a porous network is located. The lacunae of this lacunocanicular network accommodate the cell bodies of osteocytes, while their cell processes run in canaliculi. In fibrolamellar bone of minipigs, the general orientation of the canaliculi was found to be radial with tortuous and twisted pathways (Magal *et al.*, 2014).

With the simplified reconstruction approach described in this paper, we were able to reconstruct spatial distributions of mineral particle characteristics in bovine fibrolamellar bone consisting of woven bone layers augmented by lamellar layers. A spatial correlation between the mineral nanostructure and microscopic features like vascular channels demonstrated that mineral particles are particularly thin in their vicinity.

## 2. Materials and methods

### 2.1. Samples

Four matchstick-like samples of bovine bone were used for both microcomputed tomography ( $\mu\text{CT}$ ) and synchrotron scattering measurements (Fig. 1). All the samples were obtained from the femur of a 23 month old cow, obtained from a slaughterhouse. The mid-part of the diaphysis was cut into approximately 2 cm thick pieces, the endosteal cancellous bone was removed from the slice and the samples were stored at 251 K. Using a low-speed saw (Buehler Isomet, Düsseldorf, Germany) under water cooling, plate-like samples were cut under three different orientations, with the normal to the plate pointing to the radial, longitudinal and tangential directions, respectively. Each plate was then polished to roughly 150  $\mu\text{m}$  thickness. The plates were cut again to obtain stick-like samples of approximately 4 mm in length [Fig. 1(b)] with a rectangular section of about  $250 \times 150 \mu\text{m}$  [Fig. 1(c)]. The long axes of the stick-like samples were aligned with one of the main directions of the femoral bovine bone [Fig. 1(a)] and are, therefore, referred to as radial (two samples), longitudinal (one sample) and tangential (one sample).

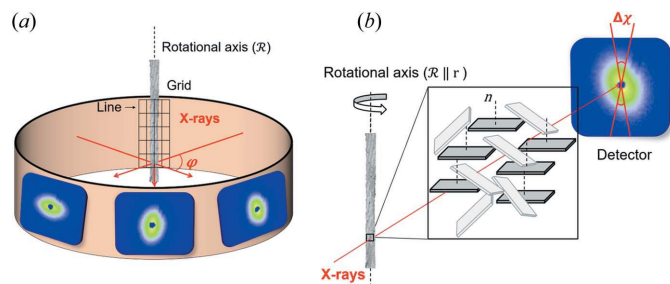


Figure 2

The experimental setup adopted for the synchrotron measurements. (a) A schematic diagram showing SAXS signals acquired at different rotational angles  $\varphi$ . (b) A  $\mu\text{CT}$  reconstruction of the sample with the rotational axis aligned to the radial direction shown in Fig. 1. In this sample, the normal to the main surface of the mineral particles is mainly parallel to the rotational axis of the sample. This allows particles to scatter the signal mainly along the vertical direction of the detector that we analyze by integrating the signal within an angular sector of  $\Delta\chi = 6^\circ$ .

### 2.2. Micro-computed tomography ( $\mu\text{CT}$ )

$\mu\text{CT}$  measurements of all four samples were performed with the EasyTom 160 (RX solutions, Chavanod, France). In each measurement, the applied tube voltage was 60 kV and the integration times (duration of each tomographic projection) 11.0 s, resulting in a voxel size of  $1.39 \mu\text{m}^3$ .

### 2.3. Synchrotron measurements

Two different synchrotron SAXS experiments were performed, on the  $\mu\text{Spot}$  beamline at BESSY II (Germany) (Paris *et al.*, 2007) and on the I22 beamline at Diamond Light Source (DLS, UK) (Smith *et al.*, 2019). Throughout this paper, reported values of the experimental settings are separated by a forward slash (/), where the first value refers to BESSY II and the second to DLS. The monochromatic X-ray beam had an energy of 18 keV/14 keV and a beam size of  $20 \mu\text{m}/10 \mu\text{m}$ , defined by a pinhole/secondary source slits. The sample-to-detector distance was about 300 mm/5495 mm. Scattered signals were acquired by an EIGER X 9M/Pilatus P3-2M detector with an exposure time of 5 s/0.5 s.

In a scanning SAXS experiment the whole width of the sample was covered by the measurement grid, with the grid step defined by the step size between measurements. In both horizontal and vertical directions, the size of the grid step was equal to the beam size. The maximum number of horizontal scanned lines in the grid was 3/25. The same SAXS scan was repeated after rotating the sample along its long axis [Fig. 2(a)]. The measured set of angles  $\theta$  ranged between  $0^\circ$  and  $180^\circ$  with an angular step of  $3^\circ/4^\circ$ . Therefore, the number of measured SAXS patterns for each sample of bovine bone was 2745/45 000.

In addition to the scattering data, X-ray attenuation data were acquired using a diode with an exposure time of 0.3 s/0.5 s. The total time for collecting a data set at BESSY was about 45 h, while for the presented data set measured at DLS the total time amounted to around 8 h.

In the scattering experiments the rotational axis  $\mathcal{R}$  of the sample coincides with the long axis of our stick-like sample.

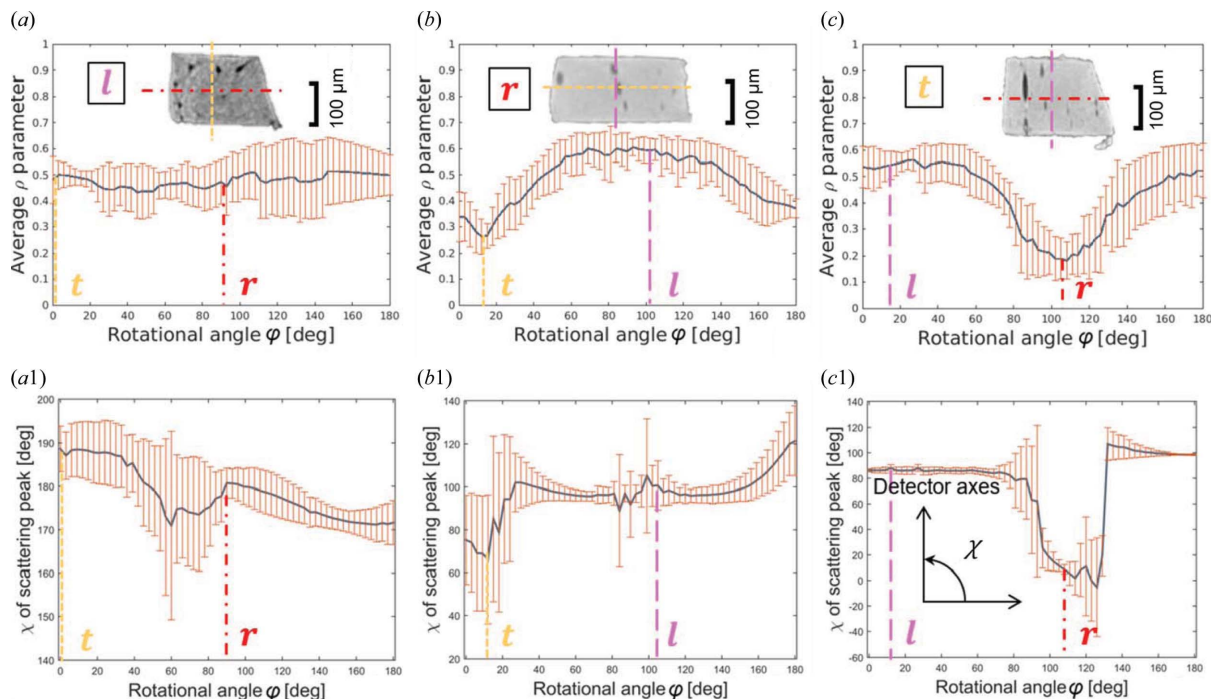


Figure 3

Macro- to nanostructure correlation. The plots show averaged values of the  $\rho$  parameter for the samples with the main axis aligned to the (a) longitudinal, (b) radial and (c) tangential directions of the samples. The values of the acquired  $\rho$  parameter at each rotational angle were averaged and the error bars indicate standard deviations. Dashed lines in each plot indicate the other two directions. (a1), (b1) and (c1) Plots of the position of the maximum of the scattering intensity ( $\chi$ ), where  $\chi$  denotes the azimuthal angle, as a function of the rotational angle  $\phi$ . **[Labels are rather fuzzy and/or small - is a revised figure available?]**

Samples were prepared in such a way that the longest extension is aligned with one of the main directions of the femoral bovine bone, *i.e.* the longitudinal, radial or tangential direction [Fig. 1(a)]. To link the rotational angle  $\theta$  of the measurement with the position of the sample in the Cartesian coordinate system defined by the longitudinal, radial and tangential directions, sinograms of the attenuation coefficients were analyzed based on the known shape of sample cross sections. As an example, for the radial sample of Fig. 3(b) the tangential direction was determined to correspond to  $\sim 12^\circ$ .

### 3. SAXS-invariant tomography

#### 3.1. SAXS invariants and platelet thickness

The SAXS intensity in 3D reciprocal space can be written as  $I(q, \chi, \phi)$ , where  $q$  is the length of the scattering vector [ $q = (4\pi/\lambda)\sin\theta$ , where  $\theta$  is half the scattering angle and  $\lambda$  is the wavelength of the incident radiation],  $\chi$  the azimuthal angle measured with respect to an axis  $\mathcal{R}$  and  $\phi$  the rotation angle around this axis  $\mathcal{R}$ . When the specimen is rotated around the axis  $\mathcal{R}$  defined by  $\chi = -\pi/2$  or  $\pi/2$ , the intensity in this direction stays unchanged since the rotation axis remains fixed during the rotation. In the case of bone where there is a strong electron density contrast between the mineral and organic phases, a two-phase model can be used to describe the small-angle scattering and  $I(q, \chi, \phi)$  is taken proportional to the function  $S(\mathbf{q})$  defined below. The proportionality constant

between the two functions will depend on instrumental parameters, as well as on the squared electron density difference between the organic and mineral phases. The vector  $\mathbf{q}$  is defined by its length  $q$  and the two angles  $\chi$  and  $\phi$ .

We consider a two-phase model with a function  $\eta(\mathbf{r})$  that is equal to 1 if there is a particle at position  $\mathbf{r}$  and is zero otherwise. Then the SAXS intensity will be proportional to

$$S(\mathbf{q}) = \frac{1}{V} \left| \int \mathbf{dr} \exp(-i\mathbf{q} \cdot \mathbf{r}) \eta(\mathbf{r}) \right|^2, \quad (1a)$$

$$= \frac{1}{V} \left| \int \mathbf{dr} \exp(-i\mathbf{q} \cdot \mathbf{r}) [\eta(\mathbf{r}) - \phi] \right|^2 \quad (\text{for } |\mathbf{q}| > 0) \quad (1b)$$

$$= \frac{1}{V} \int \mathbf{du} \exp(-i\mathbf{q} \cdot \mathbf{u}) \int \mathbf{dr} [\eta(\mathbf{r} + \mathbf{u}) - \phi] [\eta(\mathbf{r}) - \phi], \quad (1c)$$

where  $V$  is the probed volume and  $\phi$  denotes the spatial average of  $\eta$  that just equals the volume fraction of particles in the volume  $V$ . In equation (1b), note that the subtraction of  $\phi$  has no effect on  $S(\mathbf{q})$  outside the origin of reciprocal space,  $q = 0$ . However, the average of  $\eta(\mathbf{r})$  will formally generate a Dirac  $\delta$  function at the origin that is practically invisible in SAXS. Therefore, the subtraction of the constant term  $\phi$  ensures that the average of  $[\eta(\mathbf{r}) - \phi]$  over the whole volume is zero and that there is no contribution of the Dirac  $\delta$  function at  $q = 0$  (which would otherwise contribute to the analytically

calculated integral intensity). This is the usual procedure in the treatment of SAXS signals from two-phase systems, for example in solution scattering, and the spherical average of this expression is (Guinier & Fournet, 1955)

$$\begin{aligned} \bar{S}(q) &= \langle S(\mathbf{q}) \rangle \\ &= \int d\mathbf{u} \langle \exp(-i\mathbf{q} \cdot \mathbf{u}) \gamma(\mathbf{u}) \rangle \\ &= \int d\mathbf{u} \frac{\sin qu}{qu} \gamma(\mathbf{u}) \\ &= \int_0^\infty 4\pi u^2 du \frac{\sin qu}{qu} \langle \gamma(\mathbf{u}) \rangle, \end{aligned} \quad (2)$$

where the angle brackets denote the spherical average with respect to  $\mathbf{q}$  on the first two lines of the expression and with respect to  $\mathbf{u}$  on the last line. The first expression comes because only the exponential term depends on  $\mathbf{q}$ , and the second expression results from the averaging of the exponential term. In the last step, we rewrite the integration in spherical coordinates for the vector  $\mathbf{u}$ , and – since  $(\sin qu)/qu$  does not depend on angle – we remain with a single integral with respect to  $u$ , provided we replace  $\gamma$  by its spherical average with  $\bar{\gamma}$  denoting the correlation function,

$$\gamma(\mathbf{u}) = \frac{1}{V} \int d\mathbf{r} [\eta(\mathbf{r} + \mathbf{u}) - \phi][\eta(\mathbf{r}) - \phi]. \quad (3)$$

An inverse Fourier transform yields the expression for the spherically averaged correlation function (Guinier & Fournet, 1955):

$$\bar{\gamma}(u) = \gamma(\mathbf{u}) = \frac{1}{2\pi^2} \int_0^\infty q^2 dq \frac{\sin qu}{qu} \bar{S}(q). \quad (4)$$

The consequence is the first SAXS invariant, the integral intensity

$$\int_0^\infty q^2 \bar{S}(q) dq = 2\pi^2 \bar{\gamma}(0) = 2\pi^2 (\phi - \phi^2) = 2\pi^2 \phi(1 - \phi). \quad (5)$$

A Taylor expansion of the correlation function to the first order in  $u$  gives the second invariant, Porod's law (Guinier & Fournet, 1955), whereby  $S$  is the total amount of particle interface in the volume  $V$ :

$$\bar{\gamma}(u) = \phi(1 - \phi) - \frac{S}{4V} u + \dots \quad (6)$$

The Fourier transform then gives the limit of the function  $\bar{S}(q)$  for large  $q$  as

$$\bar{S}(q) \simeq \frac{S}{V} \frac{2\pi}{q^4} = \frac{P}{q^4}. \quad (7)$$

This has been used extensively [for a recent review, see Pabisch *et al.* (2013)] to determine an average thickness of particles through the parameter  $T$  defined as

$$T = \frac{4}{\pi P} \int_0^\infty q^2 \bar{S}(q) dq = \frac{4\phi(1 - \phi)}{S/V}. \quad (8)$$

Here,  $\phi$  and  $S/V$  are the volume fraction and the surface per unit volume of the particles, respectively. For thin particles with thickness  $W$ , this is well known to correspond to (Pabisch *et al.*, 2013)

$$T \simeq 2(1 - \phi)W, \quad (9)$$

so that  $T$  roughly represents the mean particle thickness for a material with a particle volume fraction close to 50% (as in bone, for example).

The goal is now to generalize these expressions for integration along a rotation axis defined by the vector  $\mathbf{q}_R = (0, 0, q_R)$ . We suppose that the specimen contains thin plates only. We first consider the contribution to the scattering by a single platelet oriented perpendicular to  $\mathbf{q}_R$  with a thickness  $W$ , and with breadth and length of  $B$  and  $L$ , respectively. Using equation (1a), the contribution of this particle to the total SAXS intensity can be written in Cartesian coordinates whereby  $z$  is along  $\mathcal{R}$ , yielding a well known result (Guinier & Fournet, 1955):

$$\begin{aligned} S_1(\mathbf{q}) &= \frac{1}{V} \left| \int_{-L/2}^{L/2} \exp(-ixq_x) dx \int_{-B/2}^{B/2} \exp(-iyq_y) dy \right. \\ &\quad \left. \times \int_{-W/2}^{W/2} \exp(-izq_z) dz \right|^2 \\ &= \frac{1}{V} L^2 B^2 W^2 \left( \frac{\sin q_x L/2}{q_x L/2} \right)^2 \left( \frac{\sin q_y B/2}{q_y B/2} \right)^2 \\ &\quad \times \left( \frac{\sin q_z W/2}{q_z W/2} \right)^2. \end{aligned} \quad (10)$$

Using the fact that the function  $(L/2\pi)[(\sin q_x L/2)/(q_x L/2)]^2$  converges to the Dirac  $\delta$  function when  $L$  gets very large, we obtain

$$S_1(\mathbf{q}) = 4\pi^2 \frac{L B W^2}{V} \left( \frac{\sin q_z W/2}{q_z W/2} \right)^2 \delta(q_x) \delta(q_y), \quad (11)$$

for  $L$  and  $B$  sufficiently large (in practical terms, larger than what SAXS would resolve in the relevant  $q$  range). Now, we call  $N_R$  the number of particles with their normal directions oriented within a small solid angle around  $\mathcal{R}$  and we denote  $f_R(W) dW$  the corresponding thickness distribution [normalized so that  $\int f_R(W) dW = 1$ ]. Then the total intensity pointing in the  $\mathcal{R}$  direction will be

$$\begin{aligned} \bar{S}_R(q_R) &= N_R \int f_R(W) dW \frac{1}{4\pi} \int_0^{2\pi} d\varphi \int_0^\pi d\chi \sin \chi S_1(\mathbf{q}) \\ &= \frac{\pi N_R L B}{q_R^2 V} \int W^2 \left( \frac{\sin q_R W/2}{q_R W/2} \right)^2 f_R(W) dW \\ &\quad (\text{for } |\mathbf{q}_R| > 0) \end{aligned} \quad (12)$$

The angles are defined such that  $q_x = q \sin \chi \cos \varphi$ ,  $q_y = q \sin \chi \sin \varphi$  and  $q_z = q \cos \chi$ , and we have neglected possible interference effects between the particles. The volume fraction of all particles perpendicular to  $\mathcal{R}$  is  $\phi_{\mathcal{R}} = N_{\mathcal{R}} L B \overline{W}_{\mathcal{R}} / V$ , where  $\overline{W}_{\mathcal{R}}$  is the average thickness of the particles. It is also worth noting that the same family of particles will also generate a similar scattering in the direction related to  $\mathcal{R}$  by an inversion symmetry with respect to the origin (meaning in the  $-\mathbf{q}_{\mathcal{R}}$  direction) but will not contribute to the scattering in any other direction.

Equation (12) can be expanded at large  $q_{\mathcal{R}}$  to give an analog to Porod's law,

$$\overline{S}_{\mathcal{R}}(q_{\mathcal{R}}) \simeq \frac{2\pi}{q_{\mathcal{R}}^4} \frac{N_{\mathcal{R}} L B}{V} = \frac{2\pi}{q_{\mathcal{R}}^4} \frac{\phi_{\mathcal{R}}}{\overline{W}_{\mathcal{R}}} = \frac{P_{\mathcal{R}}}{q_{\mathcal{R}}^4}. \quad (13)$$

Moreover, the integrated intensity along the  $\mathcal{R}$  direction (starting at the origin of  $q$  space) will be proportional to the total volume of particles perpendicular to this direction, that is, proportional to  $\phi_{\mathcal{R}}$ . The proportionality constant must be such that we recover equation (5) when summing over all possible directions. Here, we need to take into account that each plate-like particle scatters in two directions related by an inversion symmetry, so that we are counting each family of particles twice when we integrate over all directions (hence the factor 1/2 in the equation below) to get

$$\int_0^{\infty} q_{\mathcal{R}}^2 \overline{S}(q_{\mathcal{R}}) dq_{\mathcal{R}} = 2\pi^2 \frac{\phi_{\mathcal{R}}}{2} (1 - \phi). \quad (14)$$

Indeed, when we are summing this expression over all possible directions, and considering that  $\phi_{\mathcal{R}}$  and  $\phi_{-\mathcal{R}}$  refer to the same family of particles,  $\phi_{\mathcal{R}}/2$  sums up to  $\phi$ , recovering equation (5). Taking the ratio of the integral intensity above and the Porod constant in the  $\mathcal{R}$  direction,  $P_{\mathcal{R}}$ , we obtain in analogy to equation (9)

$$T_{\mathcal{R}} = \frac{4}{\pi P_{\mathcal{R}}} \int_0^{\infty} q_{\mathcal{R}}^2 \overline{S}(q_{\mathcal{R}}) dq_{\mathcal{R}} \simeq 2(1 - \phi) \overline{W}_{\mathcal{R}}. \quad (15)$$

### 3.2. SAXS data evaluation

The acquired scattering intensity on the 2D detector,  $I_a(q, \chi)$ , was corrected considering X-ray attenuation and background subtraction according to

$$I(q, \chi) = \left[ I_a(q, \chi) \frac{I_0}{I_T} \right] - I_{BG}(q, \chi), \quad (16)$$

where  $I_0$  is the intensity of the incoming beam,  $I_T$  the transmitted intensity and  $I_{BG}(q, \chi)$  the background intensity. The angle  $\chi$  is measured with respect to an axis  $\mathcal{R}$ .  $I_{BG}(q, \chi)$  was obtained by averaging the scattering pattern of three measurement points of a scan which were outside the sample. Due to the fluctuation in the beam flux during the experiments at BESSY II, a further correction was applied to the measurements using background images for normalization.

In general, this intensity is not a voxel property, since scattering crucially depends on how the nanostructural elements, like the mineral particles in bone, are oriented with respect to the incoming beam. However, the scattering pattern does not change under sample rotation along the rotational axis, *i.e.*  $I(q, \chi = -\pi/2)$  and  $I(q, \chi = \pi/2)$  are independent of the specimen rotation around  $\mathcal{R}$ . Indeed, if the sample is rotated by an angle  $\theta$  around  $\mathcal{R}$ , the reciprocal space is also rotated by the same angle around the same axis. An alternative explanation which considers the nanostructure of bone is that by focusing only on the scattered signal around the rotational axis  $\mathcal{R}$ , it is always the same subpopulation of mineral particles which contributes to the scattering signal. Taking into consideration the plate-like shape of the particles, this subpopulation consists of platelets with their normal oriented along the rotational axis [dark-gray particles in Fig. 2(b)].

For the calculation for the axial integrated intensity  $I_{\mathcal{R}}$  and the axial Porod constant  $P_{\mathcal{R}}$ , an azimuthal integration of  $I(q, \chi)$  in a very narrow sector around  $\chi = -\pi/2, \pi/2$  with an opening angle of  $\Delta\chi$  was performed. Our choice of  $\Delta\chi = 6^\circ$  proved to be a good compromise to be, on the one hand, large enough to provide a robust value for  $I_{\mathcal{R}}$  and, on the other hand, small enough to ensure that  $I_{\mathcal{R}}$  is independent of the rotational angle  $\varphi$ . The  $q$  ranges in the evaluation were  $0.2\text{--}3 \text{ nm}^{-1}/0.1\text{--}2.6 \text{ nm}^{-1}$ .

Besides the reconstruction of the  $T_{\mathcal{R}}$  parameter, a second parameter ( $\rho$  parameter), which describes the mutual alignment of the mineral particles (Pabisch *et al.*, 2013), was evaluated. To obtain the  $\rho$  parameter the SAXS patterns are radially integrated, yielding the scattered intensity as only a function of the azimuthal angle,  $I(\chi)$ . The function  $I(\chi)$  displays two peaks separated by  $180^\circ$  on top of a constant background. The  $\rho$  parameter is defined as  $\rho = A_1/(A_0 + A_1)$ , where  $A_0 + A_1$  denotes the area under the curve  $I(\chi)$  including the constant background, and  $A_1$  the area under the peaks only. Consequently, the  $\rho$  parameter takes values between 0 and 1, where 0 corresponds to a random mutual alignment and 1 to a perfect alignment of all the mineral particles.

All the SAXS data analysis was performed using the software packages *DAWN* (Basham *et al.*, 2015) and *DPDAK* (Benecke *et al.*, 2014). In order to visualize the  $\rho$  parameter as a function of the rotational angle (Fig. 3), the values of the  $\rho$  parameter acquired at a specific rotational angle were averaged.

### 3.3. Tomographic reconstructions

The essence of tomography is to reconstruct the bulk properties of a sample when only projection data are available. Typically, the different projections are obtained by scanning and rotating the sample. In the parallel-beam geometry applied in SAXS tomography experiments, reconstruction is a 2D problem defined by the slice of the sample which is scanned perpendicular to the rotational axis  $\mathcal{R}$ . In mathematical terms, projection data  $p$  are obtained at different scan-

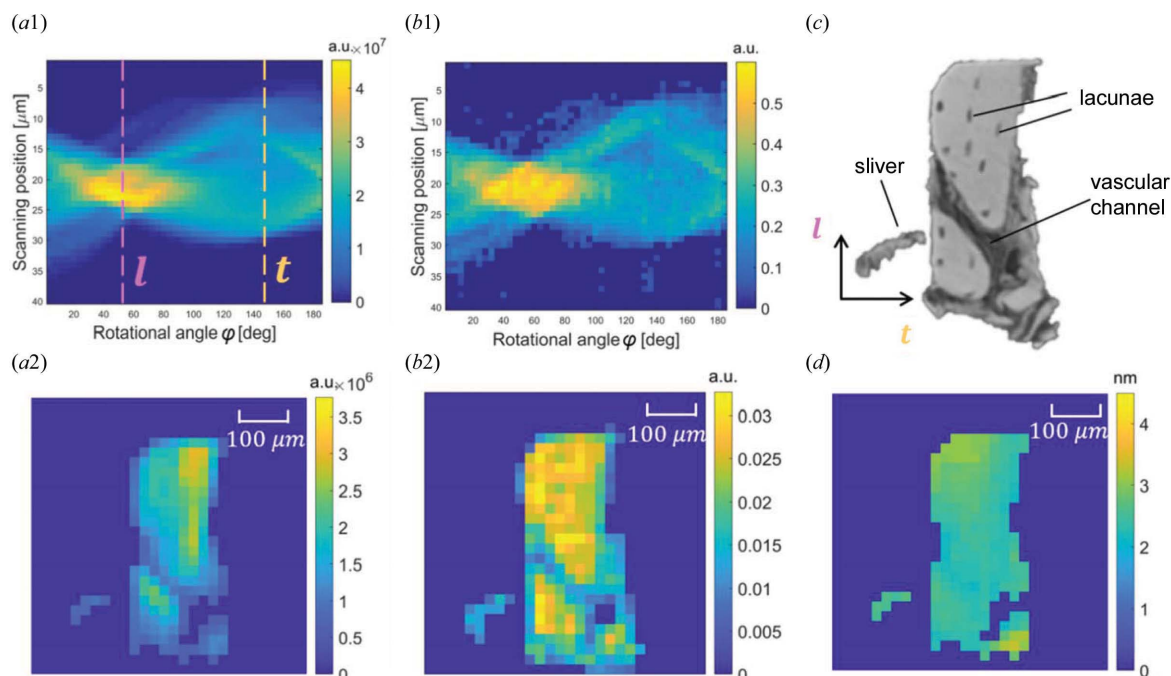


**Figure 4** Comparisons between reconstructions, using different techniques, of the region at the interface between two fibrolamellar units. (a1) A sinogram of the integrated intensity achieved from SAXS measurements. Here the longitudinal and tangential directions are marked by dashed lines. (b1) A sinogram of the quantity  $-\log(I_T/I_0)(r, \varphi)$ . (c), (a2), (b2) Reconstructions from, respectively, the  $\mu$ CT, SAXS and synchrotron CT measurements. (d) Reconstruction of the  $T_{\mathcal{R}}$  parameter map. **[Labels are rather fuzzy and/or small - is a revised figure available?]**

ning positions  $r$  and different rotational angles  $\varphi$  and are usually plotted as a function of these two variables,  $p(\varphi, r)$ , as a sinogram [see e.g. Figs. 4(a1), 4(b1)]. From these input data a material property  $m(x, y, z)$  can be inferred, where  $x$  and  $y$  are coordinates in the coordinate system of the sample and  $z$  is assumed fixed, since we consider here only the reconstruction of a 2D slice of the sample.

The reconstruction problem is solved when two requirements are fulfilled:

(i) The material property is a scalar property of the ‘voxel’ representing a small material volume and, in particular, does not depend on the angle  $\varphi$  under which the voxel is measured. The X-ray attenuation coefficient,  $\mu(x, y)$ , is such a voxel property.

(ii) The material property is an additive quantity, i.e.  $p(\theta, r) = \int_{\text{beam path}} m(x, y) ds$ .  $p(\varphi, r)$  is called the Radon transform of  $m(x, y)$ . In the case of X-ray attenuation, the Beer–Lambert law ensures that the logarithm of the measured transmitted intensity is the Radon transform of the attenuation coefficient of the material.

For each synchrotron experiment, three reconstructions were performed. From the SAXS experiments, (i) the axial integrated intensity  $I_{\mathcal{R}}$  and (ii) the axial Porod constant  $P_{\mathcal{R}}$  were reconstructed (see Section 2.3). From the X-ray attenuation experiments, (iii) the attenuation coefficient  $\mu(x, y, z)$  was reconstructed starting from measurements of the transmitted intensity, specifically  $-\log(I_T/I_0)(r, \varphi)$ . For the reconstruction, a filtered back-projection (FBP) algorithm was used (Thorsten, 2011) as implemented by the function *Iradon* in MATLAB. Due to the virtually parallel-beam

geometry, the reconstruction could be performed in ‘slices’ of the sample, where the slice has a normal identical with the rotational axis  $\mathcal{R}$  and a thickness defined by the beam size.

To perform an FBP, the type of interpolation and high-pass filtering has to be specified, which accomplishes the mapping from the polar coordinate system of the sinogram to the Cartesian one after reconstruction. From the options offered by the *Iradon* function, a spline interpolation and a Ram–Lak filter yielded the most satisfying reconstruction results. Reconstruction quality was tested by projecting the result of reconstruction (i.e. by performing a Radon transform) and calculating the mean-squared error between these projected data and the original measurement data. To avoid spurious results for the  $T$  parameter  $T_{\mathcal{R}}$  as a result of a division of two values close to zero, a threshold value for the axial integrated intensity  $I_{\mathcal{R}}$  was introduced as 16% of the maximum value of  $I_{\mathcal{R}}$  after reconstruction. All  $I_{\mathcal{R}}$  values below this threshold were set to zero. Our choice of the threshold rendered the outer shape of the sample close to results from  $\mu$ CT measurements (Section 2.2). A sensitivity analysis showed that the exact value of the threshold has a negligible influence on the reported results.

The attenuation coefficients  $\mu(x, y, z)$  were reconstructed after normalization of the data to correct for variations in the beam intensity. The data were first thresholded by setting all values of the sinogram data  $(r, \varphi) = -\log(I_T/I_0)(r, \varphi)$ , which are smaller than 6% of the maximum value equal to zero. For the normalization a factor was used which was obtained by averaging  $s(r, \varphi)$  for a fixed rotational angle. The time for the reconstruction of each slice (i.e. fixed  $z$  coordinate) for inte-



grated intensity, Porod constant and attenuation coefficient was below one second with a standard PC using FBP.

### 3.4. Spatial correlations

To allow a spatial correlation between the bone microstructure (vascular channels, osteocyte lacunae) and the mineral nanostructure, distance transforms were used. After binarizing the  $\mu$ CT image and defining the voxels in the digital image that belonged to vascular channels/osteocyte lacunae, the distance transform assigns each bone voxel in the image the shortest distance value to the defined objects. Calculations were performed in MATLAB using the function *bwdistsc*. Image registration (using the MATLAB function *imregtform*) between the  $\mu$ CT image and the 3D reconstruction of the attenuation coefficients from the synchrotron experiment was employed to map microstructure information (distance transforms) on nanostructure information (map of the  $T$  parameter).

## 4. Results

### 4.1. Correlation between mineral nanostructure and sample macrostructure

In a first step, we analyzed anisotropies of the mineral nanostructure in relation to the macroscopic coordinate system of the bovine femur defined by the longitudinal, radial and tangential directions [Fig. 1(a)]. The nanostructural anisotropy was assessed by the  $\rho$  parameter (see *Methods* section [ **$\rho$  not actually mentioned until Section 3.2?**]). Analyzed sample slices (*i.e.* cross sections through the sample with a thickness of the beam size) had their normals (which are identical to the rotational axis  $\mathcal{R}$ ) in the direction of the longitudinal, radial and tangential directions, respectively [Figs. 3(a), 3(b) and 3(c)]. For each rotational angle, a  $\rho$  parameter was calculated as the average over all measurement points in the slice [Figs. 3(a), 3(b) and 3(c)]. Different dependencies as a function of the rotational angle are observed: a rather constant curve for the longitudinal sample, while the radial and tangential samples each exhibit a minimum. These minima correlate well in position with the macroscopic directions, demonstrating that the preferred orientations of the mineral nanostructure as quantified by the  $\rho$  parameter align with the macroscopic coordinate system. The majority of mineral particles are aligned with their long axis along the longitudinal direction. Fig. 3(a1) (longitudinal sample) shows that the scattering intensity  $I(\chi)$  is a maximum at an azimuthal angle  $\chi$  of about  $180^\circ$ , independent of the rotational angle  $\varphi$ , *i.e.* perpendicular to the rotation axis, and therefore  $I_{\mathcal{R}}$  is low in the longitudinal sample. Radial samples are considered to exhibit the most effective scattering power for our SAXS tomography approach, with a position of the maximally scattered intensity near  $\chi = 90^\circ$  at most of the rotational angles  $\varphi$  and, therefore, a large value for  $I_{\mathcal{R}}$  [Fig. 3(b2) [**No such part?**]]. The majority of particles in the radial sample are oriented such that their long axes are perpendicular to the long axis of the sample and these parti-

cles contribute to the scattering signal mainly along the direction of partial integration (vertical axis of the detector in our setup), as described in Section 2.3.

### 4.2. SAXS tomography and 3D $T$ parameter map

The experimental setup allows one to obtain 3D maps by performing an independent reconstruction of sample slices (*i.e.* slices of a height equivalent to the beam size and oriented normal to the rotational axis  $\mathcal{R}$ ) and piling these slices up after reconstruction to obtain the full 3D information. Fig. 4 shows representative data for a sample slice that includes a vascular channel. In the  $\mu$ CT image of Fig. 4(c), not only can the vascular channel be clearly discerned, but osteocyte lacunae are also visible as small dark ellipsoids. A bone sliver close to the lower left corner of the sample, accidentally produced during cutting, additionally helped in the image registration of the different measurements.

Figs. 4(b1) and 4(a1) show  $s(r, \varphi)$  from the absorption measurement and the projections of the axial integrated intensity from the scattering experiment as sinogram plots (*i.e.* as a function of the rotational angle  $\varphi$  and the scanning position  $r$ , see Section 2.3). The shape of the sample contributes substantially to the values in the sinogram, with the values being highest when the sample is viewed along its diagonal. The corresponding reconstructions for the attenuation coefficient  $\mu(x, y)$  and the axial integrated intensity  $I_{\mathcal{R}}(x, y)$  are shown in Figs. 4(b2) and 4(a2), respectively. A comparison between the  $\mu$ CT image and the reconstructed attenuation coefficient shows that the synchrotron experiment allows a reliable reconstruction of the sample shape (including the sliver) and larger internal structures like vascular channels. However, the lacunae are too small to be visible.

Having reconstructed data not only for the axial integrated intensity  $I_{\mathcal{R}}$  but also for the axial Porod constant allows the determination of the thickness  $T_{\mathcal{R}}$  of mineral particles, which have their normal parallel to the rotational axis  $\mathcal{R}$ . The resulting map [Fig. 4(d)] shows spatial gradients in the particle thickness, with values above 3 nm in the upper left corner and values below 2 nm close to the vascular channel.

Repeating the evaluation for all measured sample slices and arranging the slices in the correct spatial order results in the 3D  $T_{\mathcal{R}}$  parameter map shown in Fig. 5. Values of the  $T_{\mathcal{R}}$  parameter vary between 1.7 and 4.5 nm, where regions close to the vascular channels display low values of  $T_{\mathcal{R}}$  (region in light blue). The highest values of  $T_{\mathcal{R}}$  were found within two band-like structures (regions in orange/reddish hue), with the thicknesses of the bands roughly  $40 \mu\text{m}$  and a separation between them of about  $15 \mu\text{m}$ .

### 4.3. Spatial correlation between micro- and nanostructure

The experimental design, with the same X-ray beam used to make both an absorption and a scattering experiment, allows a straightforward evaluation of spatial correlations between different structural quantities. In Fig. 6(c) the attenuation coefficient and the  $T_{\mathcal{R}}$  parameter for identical voxels in the 3D reconstructions are plotted. While  $T_{\mathcal{R}}$  reflects the nano-

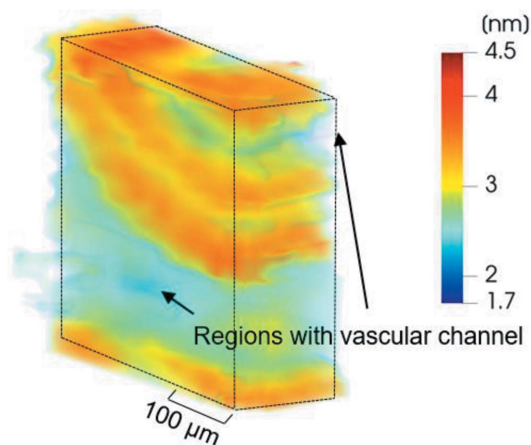


**Figure 5**  
Structural characterization of the radial sample, showing a 3D reconstructed map of the  $T_R$  parameter for the sample with its main axis aligned to the radial direction of the bovine femur.

structural thickness of the mineral particles, the attenuation coefficient provides information about the local mineral content. The data points are concentrated in two regions of the plot: thin particles ( $T_R \simeq 2.5$  nm) and low mineral content, and thicker particles ( $T_R \simeq 3.5$  nm) and higher mineral content.

Next, the mineral nanostructure is correlated with microscopic features of the fibrolamellar bone. In Fig. 6(a) the  $T_R$  parameter is plotted as a function of distance from the vascular channel. Bone close to the vascular channel exhibits particularly low values of the  $T_R$  parameter. No clear spatial

correlation can be detected when looking at the particle thickness as a function of the distance from the osteocyte lacunae [Fig. 6(b)].

In the frequency plots of Fig. 6(d) the normalized number of occurrences of the  $T_R$  parameter in both analyzed radial samples is represented. While data from the two samples with a smaller imaged volume show only one peak at relatively low values of the  $T_R$  parameter with a mean value of  $T_R = 2.81$  nm and a standard deviation (SD) of 0.23, the analogous plot of the other radial sample with the larger imaged volume exhibits two peaks of the  $T_R$  parameter, at 2.60 nm and 3.40 nm, as calculated with a Gaussian mixture model. Fig. 6(e) shows frequency plots for the longitudinal and tangential samples. For the longitudinal sample the obtained  $T_R$  parameter is relatively low (mean value 2.39 nm and SD 0.36) compared with the tangential sample (mean value 3.09 nm and SD 0.19).

### 5. Discussion and conclusions

In this proof-of-concept study on a mineralized tissue, we have demonstrated that 3D nanostructural information about mineral particle characteristics can be obtained using a new form of SAXS tomography. Our strategy was to define a quantity with contributions adding up from all the voxels that the X-ray beam passes through during the experiment, which is a voxel property independent of its orientation in relation to the X-ray beam. This strategy then allows the use of standard reconstruction methods (Thorsten, 2011) to transform the projected data into a 3D map. We have demonstrated the feasibility of this procedure for the  $T$  parameter, which is

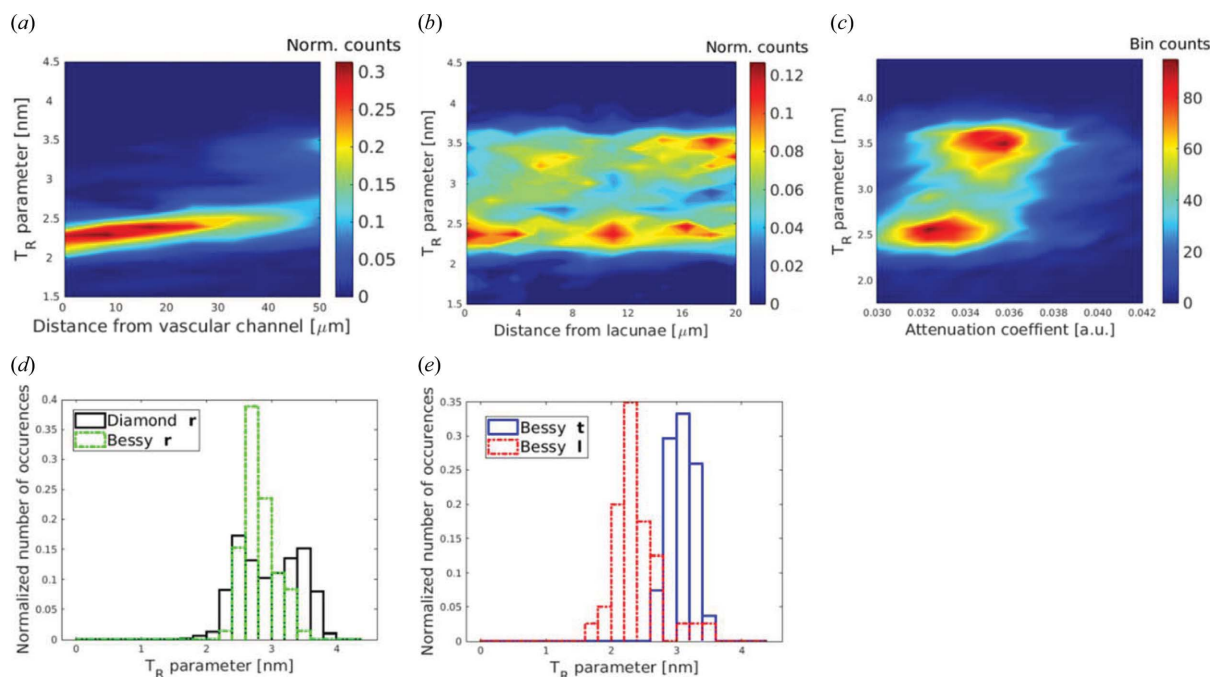


**Figure 6**  
Analyses of the reconstructed  $T_R$  parameter values. (a) The 3D distance transformation of the  $T_R$  parameter map, taking as reference the voxels containing the blood vessels. (b) The 3D distance transformation of the  $T_R$  parameter map, taking the lacunae as reference points. (c) The correlation between the  $T_R$  parameter and attenuation coefficients reconstructed from synchrotron CT measurements. (d) A normalized frequency plot of the  $T_R$  parameter distribution in the two radial samples. (e) A normalized frequency plot of the  $T_R$  parameter distribution in the tangential and longitudinal samples. **[Labels are rather fuzzy and/or small - is a revised figure available?]**

1027 calculated as the ratio of two scattering invariants, the inte- 1084  
 1028 grated intensity and the Porod constant, and which is an 1085  
 1029 important indicator of tissue maturity and its mechanical 1086  
 1030 performance. 1087

1031 A prerequisite of our approach is that the evaluated scat- 1088  
 1032 tering signal remains unchanged during the rotation of the 1089  
 1033 sample. This rotational invariance is only fulfilled for scat- 1090  
 1034 tering around the rotational axis, and consequently only 1091  
 1035 slightly more than 3% of the detector information is used in 1092  
 1036 the evaluation. This restriction of the evaluation in reciprocal 1093  
 1037 space corresponds to selecting a subpopulation of the mineral 1094  
 1038 particles in real space. Only mineral particles with a normal 1095  
 1039 parallel to the rotational axis are considered in the evaluation 1096  
 1040 and are, therefore, described by the reported  $T_{\mathcal{R}}$  parameter 1097  
 1041 (which is, for this reason, denoted with a subscript). This 1098  
 1042 specificity of our method for the particle orientation carries 1099  
 1043 implications for its usefulness. In tissues with a preferred 1100  
 1044 matrix orientation, the investigation can focus on the mineral 1101  
 1045 particles, which are embedded in the matrix in conformance 1102  
 1046 with its preferred orientation. The type of bone used in this 1103  
 1047 study – fibrolamellar bone – falls into this category, with the 1104  
 1048 fibrous collagenous matrix preferentially orientated along the 1105  
 1049 axis of the long bone. Similar to methods like polarized light 1106  
 1050 microscopy, Raman spectroscopy and second-harmonic 1107  
 1051 generation microscopy, which exploit orientational interaction 1108  
 1052 effects with collagen, our method is able to detect variations in 1109  
 1053 the alignment of mineral particles by yielding a detectable 1110  
 1054 scattering signal only if particles are ‘in plane’, *i.e.* if the 1111  
 1055 normals to their plate-like surfaces are parallel to the rota- 1112  
 1056 tional axis. 1113

1057 SAXS is an important technique to characterize the 1114  
 1058 nanostructure of inorganic–organic hybrid materials (Herwig 1115  
 1059 & Fratzl, 2006) and SAXS tomography may become a 1116  
 1060 powerful way of mapping nanostructure variations in three 1117  
 1061 dimensions within macroscopic specimens. Indeed, our 1118  
 1062 approach is not limited to biological materials like bone. While 1119  
 1063 our equations were derived for plate-like inclusions, they are 1120  
 1064 valid more generally, and  $T_{\mathcal{R}}$  is then an average chord length 1121  
 1065 of the inclusions measured in the direction  $\mathcal{R}$ . Unfortunately, 1122  
 1066 Porod’s chord-length measure does not directly describe a 1123  
 1067 particle thickness, as in the case of platelet-shaped inclusions, 1124  
 1068 but it still represents an interesting size characteristic of any 1125  
 1069 nanostructured two-phase system. 1126

1070 An issue that has to be considered when studying biological 1127  
 1071 materials with synchrotron radiation is the damage caused to 1128  
 1072 the sample by the radiation. While radiation damage in X-ray 1129  
 1073 tomographic approaches is known to affect the mechanical 1130  
 1074 properties of bone strongly, mostly by the degradation of 1131  
 1075 collagen (Barth *et al.*, 2010), the shape of mineral particles is 1132  
 1076 less affected. Although we cannot exclude the influence of 1133  
 1077 radiation damage, we did not observe a change in the SAXS 1134  
 1078 intensity from the mineral over time scales corresponding to 1135  
 1079 an experiment. 1136

1080 Our experimental setup allows the combination of several 1137  
 1081 methods using the same X-ray beam as the probe. In the 1138  
 1082 current study the beam was used to measure the absorption 1139  
 1083 coefficient, which provides information about the local 1140

1084 calcium content of the bone, together with the scattering 1085  
 1086 signal. In a similar way, the combination of methods could be 1087  
 1088 extended to include chemical analysis [*e.g.* using X-ray fluor- 1089  
 1090 escence (Lange *et al.*, 2011)]. With measurements based on the 1091  
 1092 same incoming beam, the registration of different image data 1093  
 1094 and the evaluation of the spatial correlation between different 1095  
 1096 physical quantities [like the  $T_{\mathcal{R}}$  parameter and Ca content, see 1097  
 1098 Fig. 6(c)] are straightforward. 1099

1100 An advantage of our approach is the strongly reduced effort 1101  
 1102 required for both the experimental and computational work 1103  
 1104 compared with tensor tomography, when a specific parameter 1105  
 1106 like the mineral particle thickness is sought. In the experiment, 1107  
 1108 a single rotation of the sample is sufficient to obtain recon- 1109  
 1110 structable information about the nanostructural thickness. As 1110  
 1111 a result, the size of the data set for reconstruction is reduced 1111  
 1112 and is, therefore, less demanding on the RAM of the recon- 1112  
 1113 struction computer. In addition, the reduction in the dimen- 1113  
 1114 sionality of the reconstruction problem allows the use of 1114  
 1115 standard reconstruction algorithms, which have been opti- 1115  
 1116 mized over the last few decades. Computational time can be 1116  
 1117 saved by performing the preparatory evaluation of SAXS 1117  
 1118 parameters during the measurement itself. 1118

1119 We tested our method on samples of fibrolamellar bovine 1119  
 1120 bone. The preparation of a stick-like sample oriented in the 1120  
 1121 radial direction and an imaged volume of 250  $\mu\text{m}$  in this radial 1121  
 1122 direction allowed us to image all the different layers within a 1122  
 1123 complete fibrolamellar unit. As described by Magal *et al.* 1123  
 1124 (2014), starting from a vascular channel the succession of 1124  
 1125 layers are first lamellar bone around the channel, then a 1125  
 1126 parallel-fibered layer, the primary hypercalcified layer in the 1126  
 1127 center of the fibrolamellar unit, and then again the succession 1127  
 1128 of a parallel-fibered layer and lamellar bone, before reaching 1128  
 1129 the next layer with vascular channels. Based on the  $\mu\text{CT}$  image 1129  
 1130 of our sample, we observed vascular channels close to the top 1130  
 1131 of the sample and in the lower part approximately 180  $\mu\text{m}$  1131  
 1132 apart. Due to its branching, the lower vascular channel 1132  
 1133 occupies a substantial area within a cross section of the sample 1133  
 1134 [Fig. 4(c)]. 1134

1135 Using the vascular channels as spatial references leads to 1135  
 1136 the following interpretation of the 3D  $T_{\mathcal{R}}$  parameter map of 1136  
 1137 Fig. 5: the lamellar bone around the vascular channels displays 1137  
 1138 low values of the  $T$  parameter, also clearly observable in the 1138  
 1139 spatial correlation plot [Fig. 6(a)]. The highest values of the 1139  
 1140  $T_{\mathcal{R}}$  parameters are found in two curved layers with a thickness 1140  
 1141 of 30 to 40  $\mu\text{m}$ , with the lower layer thicker than the upper 1141  
 1142 one. These two layers are interleaved with a thinner layer 1142  
 1143 ( $\sim 15 \mu\text{m}$  thick), which comprises thinner mineral particles. 1143  
 1144 The location of the layers and their thicknesses correspond 1144  
 1145 exactly to the core of the fibrolamellar unit, with the central 1145  
 1146 hypercalcified layer with a lower  $T_{\mathcal{R}}$  parameter separating the 1146  
 1147 layers of parallel-fibered bone with thick particles. The 1147  
 1148 correlation plot of Fig. 6(c) shows that the lamellar bone not 1148  
 1149 only has thinner mineral particles, but also the mineral content 1149  
 1150 is lower compared with the parallel-fibered bone. 1150

1151 The 3D map of the  $T$  parameter provides new insights into 1151  
 1152 the arrangement of the fibrolamellar units. While the lamellar 1152  
 1153 bone around the vascular channel at the bottom results in a 1153  
 1154

clear separation between the fibrolamellar units, the lamellar bone on top is quite localized around the more isolated vascular channel, which results in a more continuous transition between the two fibrolamellar units at the top. In plexiform (fibrolamellar) ovine bone, a similar correspondence of the  $T$  parameter and structural organization was found, *i.e.* relatively high  $T$  parameters in regions with a higher degree of structural organization and lower  $T$  parameters in the more woven-like areas (Kerschnitzki *et al.*, 2013). Testing different subpopulations of mineral particles showed differences in the  $T_R$  parameter [Figs. 6(*d*) and 6(*e*)]. While these measurements were performed on differently oriented samples, it is straightforward to test different subpopulations in the same sample by rotating the sample around more than one rotational axis  $\mathcal{R}$  or by reconstructing the full 3D scattering pattern (Liebi *et al.*, 2015; Schaff *et al.*, 2015). In addition, our study is limited by a low sample number. A systematic investigation of several fibrolamellar units in different locations of bovine bone and in different individuals would allow a quantitative assessment of biological variability.

The experimental approach proposed in this study provides much more information about the sample than is actually used for the reconstruction. One might also implement the idea of virtual rotation axes, originally proposed by Schaff *et al.* (2015), into this simplified treatment of SAXS data where only invariants are reconstructed. This would probably make the reconstruction of particle sizes with many orientations more effective. Furthermore, the recent past has proved that important progress in imaging techniques occurs on the computational side of the process. For our problem we see a substantial potential to exploit information from the beam profile and the availability of two data sets (scattering and attenuation) in order to improve the reconstruction result in combination with algebraic reconstruction tools (Hansen & Jørgensen, 2018).

Finally, the success of a new method is always linked to interesting applications. In investigating mineralized tissues, the most pressing problems encountered are posed by bone diseases. While mineralization disorders are often characterized in terms of the amount of mineral incorporated in the bone (Roschger *et al.*, 2008), our method would allow a mapping of structural disorders of the mineral nanostructure.

## Acknowledgements

Open access funding enabled and organized by Projekt DEAL.

## Funding information

The authors wish to acknowledge support from BiGmax, the Max Planck Society's Research Network on Big-Data-Driven Materials Science. We also acknowledge Diamond Light Source for the generous award of beamtime (SM18524-2). H. S. Gupta thanks the Biotechnology and Biological Sciences Research Council (grant No. BB/R003610/1) and UK Research and Innovation (grant No. MR/R025673/1) for research grant funding.

## References

- Bar-On, B. & Wagner, H. D. (2013). *J. Struct. Biol.* **183**, 149–164.
- Barth, H. D., Launey, M. E., MacDowell, A. A., Ager, J. W. III & Ritchie, R. O. (2010). *Bone*, **46**, 1475–1485.
- Basham, M., Filik, J., Wharmby, M. T., Chang, P. C. Y., El Kassaby, B., Gerring, M., Aishima, J., Levik, K., Pulford, B. C. A., Sikharulidze, I., Sneddon, D., Webber, M., Dhesi, S. S., Maccherozzi, F., Svensson, O., Brockhauser, S., Náray, G. & Ashton, A. W. (2015). *J. Synchrotron Rad.* **22**, 853–858.
- Benecke, G., Wagermaier, W., Li, C., Schwartzkopf, M., Flucke, G., Hoerth, R., Zizak, I., Burghammer, M., Metwalli, E., Müller-Buschbaum, P., Trebbin, M., Förster, S., Paris, O., Roth, S. V. & Fratzl, P. (2014). *J. Appl. Cryst.* **47**, 1797–1803.
- Bouville, F., Maire, E., Meille, S., Van de Moortèle, B., Stevenson, A. J. & Deville, S. (2014). *Nat. Mater.* **13**, 508–514.
- Buzug & Thorsten, M. (2011). *Handbook of Medical Technology: Computed Tomography*. Heidelberg; Springer.
- Feldkamp, J. M., Kuhlmann, M., Roth, S. V., Timmann, A., Gehrke, R., Shakhverdova, I., Paufler, P., Filatov, S. K., Bubnova, R. S. & Schroer, C. G. (2009). *Phys. Status Solidi A*, **206**, 1723–1726.
- Filik, J., Ashton, A. W., Chang, P. C. Y., Chater, P. A., Day, S. J., Drakopoulos, M., Gerring, M. W., Hart, M. L., Magdysyuk, O. V., Michalik, S., Smith, A., Tang, C. C., Terrill, N. J., Wharmby, M. T. & Wilhelm, H. (2017). *J. Appl. Cryst.* **50**, 959–966.
- Fratzl, P., Fratzl-Zelman, N., Klaushofer, K., Vogl, G. & Koller, K. (1991). *Calcif. Tissue Int.* **48**, 407–413.
- Fratzl, P. & Weinkamer, R. (2007). *Mater. Sci.* **52**, 1263–334.
- Fratzl-Zelman, N., Schmidt, I., Roschger, P., Glorieux, F. H., Klaushofer, K., Fratzl, P., Rauch, F. & Wagermaier, W. (2014). *Bone*, **60**, 122–128.
- Gao, Z., Guizar-Sicairos, M., Lutz-Bueno, V., Schröter, A., Liebi, M., Rudin, M. & Georgiadis, M. (2019). *Acta Cryst. App.* **75**.
- Georgiadis, M., Guizar-Sicairos, M., Gschwend, O., Hangartner, P., Bunk, O., Müller, R. & Schneider, P. (2016). *PLoS One*, **11**, e0159838.
- Georgiadis, M., Guizar-Sicairos, M., Zwahlen, A., Trüssel, A. J., Bunk, O., Müller, R. & Schneider, P. (2015). *Bone*, **71**, 42–52.
- Guinier, A. & Fournet, G. (1955). *Small-angle Scattering of X-rays*. New York: Wiley.
- Hansen, P. C. & Jørgensen, J. S. (2018). *Numer. Algor.* **79**, 107–137.
- He, F., Chiou, A. E., Loh, H. C., Lynch, M., Seo, B. R., Song, Y. H., Lee, M. J., Hoerth, R., Bortel, E. L., Willie, B. M., Duda, G. N., Estroff, L. A., Masic, A., Wagermaier, W., Fratzl, P. & Fischbach, C. (2017). *Proc. Natl Acad. Sci. USA*, **114**, 10542–10547.
- Herwig, P. & Fratzl, P. (2006). *Monatsh. Chem.* **137**, 529–543.
- Jäger, I. & Fratzl, P. (2000). *Biophys. J.* **79**, 1737–1746.
- Jaschouz, D., Paris, O., Roschger, P., Hwang, H.-S. & Fratzl, P. (2003). *J. Appl. Cryst.* **36**, 494–498.
- Jensen, T. H., Bech, M., Bunk, O., Thomsen, M., Menzel, A., Bouchet, A., Le Duc, G., Feidenhans'l, R. & Pfeiffer, F. (2011). *Phys. Med. Biol.* **56**, 1717–1726.
- Kerschnitzki, M., Kollmannsberger, P., Burghammer, M., Duda, G. N., Weinkamer, R., Wagermaier, W. & Fratzl, P. (2013). *J. Bone Miner. Res.* **28**, 1837–1845.
- Lange, C. C., Li, I., Manjubala, W., Wagermaier, J., Kühnisch, M., Kolanczyk, S., Mundlos, P., Knaus, P. & Fratzl, P. (2011). *J. Struct. Biol.* **176**, 159–167.
- Liebi, M., Georgiadis, M., Kohlbrecher, J., Holler, M., Raabe, J., Usov, I., Menzel, A., Schneider, P., Bunk, O. & Guizar-Sicairos, M. (2018). *Acta Cryst. A* **74**, 12–24.
- Liebi, M., Georgiadis, M., Menzel, A., Schneider, P., Kohlbrecher, J., Bunk, O. & Guizar-Sicairos, M. (2015). *Nature*, **527**, 349–352.
- Magal, Almany, R., Reznikov, N., Shahar, R. & Weiner, S. (2014). *J. Struct. Biol.* **186**, 253–64.
- Meyers, M. A., Chen, P.-Y., Lin, A. Y.-M. & Seki, Y. (2008). *Prog. Mater. Sci.* **53**, 1–206.

1255 Milovanovic, P., Zimmermann, E. A., Riedel, C., vom Scheidt, A.,  
 1256 Herzog, L., Krause, M., Djonc, D., Djuric, M., Püschel, K. &  
 1257 Amling, M. (2015). *Biomaterials*, **45**, 46–55. 1312  
 1258 Pabisch, S., Wagermaier, W., Zander, T., Li, C. & Fratzl, P. (2013).  
 1259 *Methods in Enzymology*, **Vol.2, Vol. title and editors? Chapter?,**  
 1260 **Page range?.** Amsterdam; Elsevier. **[Please complete reference]** 1313  
 1261 Paris, O., Li, C., Siegel, S., Weseloh, G., Emmerling, F., Riesemeier, H.,  
 1262 Erko, A. & Fratzl, P. (2007). *J. Appl. Cryst.* **40**, s466–s470. 1314  
 1263 Paris, O. I., Zizak, H., Lichtenegger, P., Roschger, K., Klaushofer, K.  
 1264 & Fratzl, P. (2000). *Cell. Mol. Biol.* **46**, 993–1004. 1315  
 1265 Pathi, S. P., Lin, Debra D. W., Dorvee, J. R., Estroff, L. A. &  
 1266 Fischbach, C. (2011). *Biomaterials*, **32**, 5112–5122. 1316  
 1267 Rinnerthaler, S. P., Roschger, P., Jakob, H. F., Nader, K., Klaushofer,  
 1268 K. & Fratzl, P. (1999). *Calcif. Tissue Int.* **64**, 422–429. 1317  
 1269 Ritchie, R. O. (2011). *Nat. Mater.* **10**, 817–822. 1318  
 1270 Roschger, P., Paschalis, E. P., Fratzl, P. & Klaushofer, K. (2008). *Bone*,  
 1271 **42**, 456–466. 1319  
 1272 Roschger, P., Grabner, B. M., Rinnerthaler, W., Tesch, M., Kneissel,  
 1273 A., Berzlanovich, K., Klaushofer, K. & Fratzl, P. (2001). *J. Struct.*  
 1274 *Biol.* **136**, 126–136. 1320  
 1275 Schaff, F., Bech, M., Zaslansky, P., Jud, C., Liebi, M., Guizar-Sicairos,  
 1276 M. & Pfeiffer, F. (2015). *Nature*, **527**, 353–356. 1321  
 1277 Schroer, C. G., Kuhlmann, M., Roth, S. V., Gehrke, R., Stribeck, N.,  
 1278 Almendarez-Camarillo, A. & Lengeler, B. (2006). *Appl. Phys. Lett.*  
 1279 **88**, 164102. 1314  
 1280 Seidel, R., Gourrier, A., Kerschnitzki, M., Burghammer, M., Fratzl, P.,  
 1281 Gupta, H. S. & Wagermaier, W. (2012). *Biointerphases* **1**, 123–131. 1315  
 1282 Seto, J., Gupta, H. S., Zaslansky, P., Wagner, H. D. & Fratzl, P. (2008).  
 1283 *Adv. Funct. Mater.* **18**, 1905–1911. 1316  
 1284 Smith, A. J., Davidson, L. S., Emmins, J. H., Bardsley, J. C. P.,  
 1285 Holloway, M., Marshall, M. A. R., Pizzey, C. L., Rogers, S. E. &  
 1286 Shebanova, O. (2019). arXiv:1903.05405. 1317  
 1287 Studart, A. R. (2013). *Adv. Funct. Mater.* **23**, 4423–4436. 1318  
 1288 Wagermaier, W. H. S., Gupta, A., Gourrier, M., Burghammer, P.,  
 1289 Roschger & Fratzl, P. (2006). *Biointerphases*, **1**, 1–5. 1319  
 1290 Weiner, S., Traub, W. & Wagner, H. D. (1999). *J. Struct. Biol.* **126**, 241–  
 1291 255. 1320  
 1292 Weiner, S. & Wagner, H. D. (1998). *Annu. Rev. Mater. Sci.* **28**, 271–  
 1293 298. 1321  
 1294 Weinkamer, R. & Fratzl, P. (2016). *MRS Bull.* **41**, 667–671. 1322  
 1295 Xi, L., Paolino De Falco, E., Barbieri, A., Karunaratne, L., Bentley,  
 1296 C. T. E., Terrill, N. J., Brown, S. D. M., Cox, R. D. & Davis, G. R.  
 1297 (2018). *Acta Biomater.* **76**, 295–307. 1323  
 1298 Zizak, I. P., Roschger, O., Paris, O., Misof, B. M., Berzlanovich, S.,  
 1299 Bernstorff, H., Amenitsch, K., Klaushofer, K. & Fratzl, P. (2003). *J.*  
 1300 *Struct. Biol.* **141**, 208–217. 1324  
 1301 1325  
 1302 1326  
 1303 1327  
 1304 1328  
 1305 1329  
 1306 1330  
 1307 1331  
 1308 1332  
 1309 1333  
 1310 1334  
 1311 1335  
 1312 1336  
 1313 1337  
 1314 1338  
 1315 1339  
 1316 1340  
 1317 1341  
 1318 1342  
 1319 1343  
 1320 1344  
 1321 1345  
 1322 1346  
 1323 1347  
 1324 1348  
 1325 1349  
 1326 1350  
 1327 1351  
 1328 1352  
 1329 1353  
 1330 1354  
 1331 1355  
 1332 1356  
 1333 1357  
 1334 1358  
 1335 1359  
 1336 1360  
 1337 1361  
 1338 1362  
 1339 1363  
 1340 1364  
 1341 1365  
 1342 1366  
 1343 1367  
 1344 1368



ISSN: 1600-5767

YOU WILL AUTOMATICALLY BE SENT DETAILS OF HOW TO DOWNLOAD AN ELECTRONIC REPRINT OF YOUR PAPER, FREE OF CHARGE. PRINTED REPRINTS MAY BE PURCHASED USING THIS FORM.

Please scan your order and send to [ls@iucr.org](mailto:ls@iucr.org)

INTERNATIONAL UNION OF CRYSTALLOGRAPHY

5 Abbey Square  
Chester CH1 2HU, England.

VAT No. GB 161 9034 76

Article No.: J210088-VG5128

Title of article Tomographic X-ray scattering based on invariant reconstruction – analysis of the 3D nanostructure of bovine bone

Name Wolfgang Wagermaier

Address Department of Biomaterials, Max Planck Institute of Colloids and Interfaces, Potsdam 14476, Germany

E-mail address (for electronic reprints) [wolfgang.wagermaier@mpikg.mpg.de](mailto:wolfgang.wagermaier@mpikg.mpg.de)

OPEN ACCESS

Your article appears to qualify for open-access publication at no charge under a transformative deal with the institution of your corresponding author. For more information on open-access arrangements for this journal, please go to <https://journals.iucr.org/j/services/openaccess.html>.

DIGITAL PRINTED REPRINTS

I wish to order . . . . . paid reprints

These reprints will be sent to the address given above. If the above address or e-mail address is not correct, please indicate an alternative:

[Empty box for alternative address]

PAYMENT (REPRINTS ONLY)

Charge for reprints . . . . . USD

An official purchase order made out to INTERNATIONAL UNION OF CRYSTALLOGRAPHY  is enclosed  will follow

Purchase order No. [ ]

Please invoice me

I wish to pay by credit card

EU authors only: VAT No: [ ]

Date | Signature

## DIGITAL PRINTED REPRINTS

An electronic reprint is supplied free of charge.

Printed reprints without limit of number may be purchased at the prices given in the table below. The requirements of all joint authors, if any, and of their laboratories should be included in a single order, specifically ordered on the form overleaf. All orders for reprints must be submitted promptly.

Prices for reprints are given below in **United States dollars** and include postage.

Number of reprints required	Size of paper (in printed pages)				
	1–2	3–4	5–8	9–16	Additional 8's
50	184	268	372	560	246
100	278	402	556	842	370
150	368	534	740	1122	490
200	456	664	920	1400	610
Additional 50's	86	128	178	276	116

## PAYMENT AND ORDERING

Official purchase orders should be made out to **INTERNATIONAL UNION OF CRYSTALLOGRAPHY**.

Orders should be returned by email to [ls@iucr.org](mailto:ls@iucr.org)

## ENQUIRIES

Enquiries concerning reprints should be sent to [support@iucr.org](mailto:support@iucr.org).